Using Molten Salts to Probe Outer-Coordination Sphere Effects on Lanthanide(III)/(II) Electron-Transfer Reactions

Using Molten Salts to Probe Outer-Coordination Sphere Effects on Lanthanide(III)/(II) Electron-Transfer Reactions

Molly M. MacInnes,[1] Zachary R. Jones,[1] Bo Li,[1] Nickolas H. Anderson,[1,*] Enrique R. Batista,[1,*] Ida M. DiMucci,[1] Cecilia Eiroa-Lledo,[1] Karah E. Knope,[2] Maksim Y. Livshits,[1] Stosh A. Kozimor,[1,*] Veronika Mocko,[1] Kristen A. Pace,[1] Francisca R. Rocha,[1] Benjamin W. Stein,[1,*] Jennifer N. Wacker[1,2] Ping Yang.[1,*]

[1]   Los Alamos National Laboratory (LANL), P.O. Box 1663, Los Alamos, New Mexico, 87545, USA

[2]   Department of Chemistry, Georgetown University, 37th and O Streets NW, Washington, D.C. 20057, USA

*   To whom correspondence should be directed, *e-mail;* *stosh@lanl.gov, nhanderson@lanl.gov, bstein@lanl.gov, erb@lanl.gov, pyang@lanl.gov*

Abstract:

Controlling structure and reactivity by manipulating the outer-coordination sphere around a given reagent resents a longstanding challenge in chemistry. Despite

advances toward solving this problem, it remains difficult to experimentally interrogate and characterize outer-coordination sphere impact. This work describes an alternative approach that quantifies outer-coordination sphere effects. It shows how molten salt metal chlorides (MCl_n; M = K, Na, n = 1; M = Ca, n = 2) provided excellent platforms for experimentally characterizing the influence of the outer-coordination sphere cations (M^{n+}) on redox reactions accessible to lanthanide ions; $Ln^{3+} + e^{1-} \rightarrow Ln^{2+}$ (Ln = Eu, Yb, Sm; e^{1-} = electron). As a representative example, X-ray absorption spectroscopy and cyclic voltammetry results showed that Eu^{2+} instantaneously formed when Eu^{3+} dissolved in molten chloride salts that had strongly polarizing cations (like Ca^{2+} from $CaCl_2$) via the $Eu^{3+} + Cl^{1-} \rightarrow Eu^{2+} + \frac{1}{2} Cl_2$ reaction. Conversely, molten salts with less polarizing outer-sphere M^{1+} cations (e.g. K^{1+} in KCl) stabilized Ln^{3+}. For instance, the Eu^{3+}/Eu^{2+} reduction potential was >0.5 V more positive in $CaCl_2$ than in KCl. In accordance with first-principles molecular dynamics (FPMD) simulations, we postulated that hard M^{n+} cations (high polarization power) inductively removed electron density from Ln^{n+} across $Ln-Cl\cdots M^{n+}$ networks and stabilized electron-rich and low oxidation

2

state Ln^{2+} ions. Conversely, less polarizing M^{n+} cations (like K^{1+}) left electron density on Ln^{n+} and stabilized electron-deficient and high-oxidation state Ln^{3+} ions.

INTRODUCTION

Understanding how chemical characteristics within the *primary* coordination sphere of a given analyte are influenced by the *secondary* (and subsequently outer-lying) coordination sphere represents a longstanding scientific challenge. It is now known that the outer-coordination sphere plays a critical role in directing inner-sphere characteristics for many important materials and compounds. The most well-known example comes from metalloenzyme and protein function.[1–4] However, the importance of the outer-coordination sphere spans beyond this realm. The outer-coordination sphere directs structure and properties of metals[5,6] and catalysts,[7–11] influences the conductivity, optical, and magnetic properties of solid-state materials and molecules,[12–15] and is important in the design of organic molecules for ligands and extractants.[16–23] Despite numerous advances on this front, what remains unknown is how to purposefully control and use the outer-coordination sphere to tune coordination chemistry around the central metal cation. This gap could be closed if the influence of the outer-coordination sphere were better understood. Unfortunately, it is difficult to quantitatively characterize how the outer-coordination sphere impacts structure and reactivity, both experimentally and computationally. This leaves researchers speculating about which outer-coordination sphere attributes are important to consider. The end result is unvalidated computational models and scientific debate.

Herein, we present a unique approach for characterizing the influence of the outer-coordination sphere. We identified molten salts as an ideal testbed. Within a molten salt, cations

in the outer-coordination sphere are connected across an anionic linker within the inner-coordination sphere to a dissolved metal ion, Scheme 1. Changing the identity of the molten salt cation can provide insight into the outer-coordination sphere impact on the chemistry accessible to the central metal. Previous reports have shown that the reactivity – especially electron transfer chemistry – of rare earth and actinide metal ions can be greatly influenced by their coordination environments.[24–32] Consider, in particular, published electrochemistry and calorimetry measurements that showed rare earth electron transfer chemistry and thermodynamic properties (Gibbs free energy) correlated with the molten salt cation identity.[33–41] Often, these observations are rationalized based on differences in lanthanide speciation within a given salt (LnX_n^{3-n}) and by evaluating acidity vs. basicity properties of the aprotic melts. Within this framework, *DUFFY* and *INGRAM* developed and used an "optical basicity scale" as a guide to explain ionic interactions in glasses and molten salts.[42]

Building upon those pioneering efforts, we present additional insight and use the molten salt platform to interrogate the influence of the molten salt cation – which resides in the outer-coordination sphere – over *f*-element electron transfer chemistry. We observed using a combination of X-ray absorption near edge spectroscopy (XANES), cyclic voltammetry, and first-principles molecular dynamics (FPMD) simulations that the molten salt cation identity substantially impacted electron transfer chemistry available to lanthanides, specifically in terms of the $Ln^{3+} + e^{1-} \rightarrow Ln^{2+}$ (Ln = Eu, Yb, and Sm) reaction. The results provide a proof-of-principle for rationalizing how Ln^{3+}/Ln^{2+} redox potentials could be tuned widely as a function of the molten salt cation's polarization power. Polarization power is defined as the oxidation state of the molten salt cation divided by the square of its ionic radius [oxidation state ÷ (ionic radius)^2] and essentially correlates with cationic hardness or softness.[43–45] Our interpretation is

expansive in that it provides an intuitive method for rationalizing, predicting, and controlling f-element redox chemistry in terms of outer-coordination sphere influence over Ln^{n+} redox chemistry. The results are presented in the context of analogous measurements made in aqueous solutions, which, in turn, highlighted the utility of the molten salt as a platform for characterizing outer-coordination sphere effects on one of the most important chemical transformations known: the electron transfer reaction.

Results and Discussion

Lanthanide L$_3$-edge X-ray Absorption Near Edge Spectroscopy (XANES). To interrogate

dependence of electron transfer chemistry accessible to lanthanide (Ln) cations as a function of molten salt identity, anhydrous lanthanide(III) trichlorides (LnCl$_3$, Ln = Eu, Yb, Sm) were dissolved in a series of molten alkali and alkaline chloride salts. These LnCl$_3$ compounds were selected because the Ln^{3+}/Ln^{2+} reduction potentials span a wide range. For instance, Eu^{2+} is a moderate reducing agent (reduction potential, $E_{\frac{1}{2}}$ = −0.55 V vs. Ag/AgCl in non-complexing aqueous solutions),[46] Yb^{2+} is an intermediate reducing agent (reduction potential = −1.2 V vs. Ag/AgCl),[47] and Sm^{2+} is a strong reducing agent ($E_{\frac{1}{2}}$ = −2.0 V vs. Ag/Ag^{1+} in THF).[48]

Samples were prepared by grinding the LnCl$_3$ analytes with the corresponding salt (CaCl$_2$, NaCl, and KCl) using a mortar and pestle. This intimate mixture (10% by weight in LnCl$_3$) was transferred to an uncapped aluminum oxide (Al$_2$O$_3$) crucible and subsequently heated (1 °C/min to 850 °C) in a muffle furnace that was housed within an argon filled glovebox. After maintaining the temperature at 850 °C for 12 h, the sample was cooled to room temperature (1 °C/min) and the resulting lanthanide-containing salt pucks were freed by smashing the crucible

with a hammer. We postulated that after the heating and cooling cycle, in some cases, electron transfer reactions had occurred based on the product colors. For example, reactions with $EuCl_3$ turned purple in NaCl and were white in KCl and $CaCl_2$. Reactions with $SmCl_3$ turned purple in NaCl and $CaCl_2$ and pale yellow in KCl. Reactions with $YbCl_3$ turned light brown. We also observed that the glovebox had to be rigorously free of organic solvents. Omission of any of these details caused deleterious side reactions that generated black solids, which were consequently difficult to characterize.

The samples were then characterized at room temperature using lanthanide L_3-edge X-ray absorption near edge spectroscopy (XANES). The Ln L_3-edge XANES technique represents one of the most diagnostic methods for characterizing lanthanide oxidation states because the ca. 8 eV difference between the Ln^{3+} and Ln^{2+} absorption peaks is easily resolved.[49–52] Background-subtracted and normalized XANES spectra from the above-mentioned mixtures were compared against analogous measurements made on the well-defined $LnCl_3$ and $LnCl_2$ oxidation state standards (Figure 1 and Table 1). Each spectrum displayed intense absorption peaks superimposed on absorption thresholds. Peak positions were characterized by their peak maxima and inflection points, where the first and second derivatives of the data equaled zero, respectively.

The Eu L_3-edge XANES results showed that reduction of $EuCl_3$ to Eu^{2+} occurred when heated in molten alkali metal and alkaline earth salts ($CaCl_2$, NaCl, KCl), albeit completeness of the reduction varied with molten salt identity. For example, heating $EuCl_3$ in $CaCl_2$ generated a product that almost exclusively contained europium in the +2 oxidation state (there were negligible contributions from the Eu^{3+}). In the XANES experiment, this manifested as an intense low-energy feature (inflection point = 6,973.6 eV) that occurred at nearly the same energy as the

+2 oxidation-state standard (EuCl$_2$; inflection point = 6,973.7 eV; Figure 1 and Table 1). Only a small high-energy peak at 6,982.1 eV (maximum) attributable to the +3 oxidation state (EuCl$_3$ at 6,983.7 eV, maximum) was detected. Notice that the energy axis in Figure 1 was plotted so that zero marks the inflection point from the lanthanide +3 standard, which in this case was EuCl$_3$.

Changing the identity of molten salt from a small dication with high-polarization power (Ca^{2+}; strong Lewis acid) to the larger monocation (Na^{1+}; weaker Lewis acid) imparted notable changes in the Eu L$_3$-edge XANES data. Compared to the CaCl$_2$ example, the intensity for the peak corresponding to Eu^{2+} (6,974.3 eV; inflection point) decreased in NaCl and the intensity of the Eu^{3+} peak (6,983.6 eV, maximum) increased. The nearly equivalent Eu^{3+} and Eu^{2+} peak intensities suggested that (*1*) the sample contained approximately equal amounts of Eu^{3+} and Eu^{2+} and (*2*) reduction to Eu^{2+} occurred to a larger extent when EuCl$_3$ was dissolved in molten CaCl$_2$ vs. NaCl. Moving next from Na^{1+} to K^{1+} – even lower polarization power (weaker Lewis acid) – generated a product that contained almost exclusively Eu^{3+}. This spectrum was similar to the +3 oxidation state standard (EuCl$_3$) in that it displayed a high-energy absorption peak at 6,983.9 eV (maximum); although, a small feature at low-energy (6,974.1 eV, inflection point) similar to that from EuCl$_2$ was also present. We proposed that Eu^{2+} formed at high temperature in these salts via the Eu^{3+} + Cl^{1-} → Eu^{2+} + ½ Cl$_2$ redox transformation.

The reduction (Ln^{3+} + e^{1-} → Ln^{2+}) that generated Eu^{2+} when EuCl$_3$ dissolved in molten salts (described above) did not generally occur with Yb and Sm to any appreciable extent (Figure 1, Table 1). This was likely related to differences in reduction potentials; Yb^{2+} and Sm^{2+} are much stronger reducing agents and (in general) more difficult to access synthetically.[53,54] As testament, for samarium, whose +2 oxidation state was the strongest reducing agent, the Sm L$_3$-edge XANES spectra obtained from the products that formed after heating (at 850 °C) SmCl$_3$ in NaCl

and KCl salts contained only one peak each. Inflection point energies for these absorption peaks

(6,720.8 and 6,720.6 eV, respectively) were nearly equivalent to the $SmCl_3$ standard energy (at

6,721.1 eV, which was shifted to zero in Figure 1). The Sm L_3-edge XANES data from the

$SmCl_3$ in $CaCl_2$ reaction product was similar in that the spectrum also contained a large and

dominant absorption peak at 6,721.0 eV. However, closer inspection revealed a small Sm^{2+}

feature near 6,714.0 eV (approximately 7 eV below the absorption peak) that was likely

associated with a small amount of Sm^{2+} reduction product.[49,55] For ytterbium – whose $Yb^{3+/2+}$

redox couple is between those of $Eu^{3+/2+}$ and $Sm^{3+/2+}$ – the results were bracketed by the

europium and samarium examples. In KCl, there was no evidence of Yb^{2+} and only a single Yb^{3+}

absorption peak was present at 8,946.7 eV. In NaCl, a small feature attributable to Yb^{2+} was

evident (near 8,941 eV) at the onset of the Yb^{3+} absorption peak's (8,947.0 eV) rising edge.

Finally, in $CaCl_2$, both Yb^{3+} and Yb^{2+} were observed. A small peak associated with Yb^{2+} was

clearly present (8,940.5 eV) as was the Yb^{3+} feature (8,947.3 eV).

Molten Salt Voltammetry. To further evaluate dependence of lanthanide electron transfer

reactions on molten salt identity, the $Ln^{3+} + e^{1-} \rightarrow Ln^{2+}$ (Ln = Eu, Yb, Sm) reduction potentials

were evaluated using cyclic voltammetry *in situ,* at elevated temperatures (850 °C), and as a

function of the molten salt identity (KCl, NaCl, and $CaCl_2$). For these experiments the alkali

metal or alkaline earth salt (2.5 g) was heated (850 °C) above its melting point in a high-

temperature electrochemical cell (quartz test tube) that was inside a custom-made furnace (see

Methods section and Supporting Information). After ensuring the potential of the reference

electrode was stable and that no redox activity occurred within the solvent potential window

8

(Supporting Information), solid $LnCl_3$ (0.025 g, 1% by weight) was dropped into the cell. The solution was then stirred manually with the electrodes. After settling for about 5 min, voltammetry experiments were conducted. All electrochemical experiments in molten salts used glassy carbon rods as the working and counter electrodes. As established previously, Ag/AgCl (1% wt. AgCl in the corresponding chloride salt) provided a reference electrode that enabled comparison between the electrochemical measurements.[56–61] The Ag/AgCl reference electrode is one of the best reference systems for electrochemical measurements in molten salts. We refer the interested reader to Chapter 7 of the *Handbook of Reference Electrodes* where detailed descriptions of advantages and limitations of this molten salt reference system can be found.[61] Electrochemical data were compared in Figure 2 and Table 2 and scan rate dependence documented in the Supporting Information. For this discussion, we begin by describing the results from $EuCl_3$ in detail and conclude by comparing those data with measurements made on $YbCl_3$ and $SmCl_3$.

The voltammogram of $EuCl_3$ dissolved in molten KCl (Figure 2, top pane, purple trace) showed a quasi-reversible wave with a reduction potential ($E_{1/2}$) of +0.554 ± 0.004 V and a peak separation (ΔE_p) of 328 ± 9 mV (average of three replicates at 1 V/sec). Note: the $E_{1/2}$ values reported here were determined by finding the midpoint between the peaks of the cathodic and anodic waves. Both cathodic and anodic waves were well separated from the edge of the solvent window (near 1.1 V where Cl^{1-} oxidation to Cl_2 occurred). We attributed this electrochemical event to the quasi-reversible $Eu^{3+} + e^{1-} \rightarrow Eu^{2+}$ one electron reduction. Changing the molten salt from K^{1+} to Na^{1+} imparted changes on the voltammogram (Figure 2, top pane, green trace). There were small variances that were likely attributable to thermal conductivity, electrical conductivity, and viscosity differences between KCl and NaCl (thermal conductivity and

viscosity affect convection and diffusion).[60] For example, the peak separation (ΔE_p) was nearly twice as large in NaCl (620 ± 50 mV) vs. KCl (328 ± 9 mV) at 1 V/sec, and the cathodic and anodic current plateaued rather than peaked in NaCl. The change in ΔE_p may also have some contribution from differences in Na^{1+} binding to Cl^{1-} compared to K^{1+} binding to Cl^{1-}.[62] It should also be noted that the voltammetry experiments were not corrected for uncompensated resistance. The most glaring difference was that the presence of Na^{1+} substantially shifted the Eu^{3+}/Eu^{2+} reduction potential by more than +100 mV from that observed in KCl, from +0.554 ± 0.004 V to +0.67 ± 0.04 V. Changing the salt cation from Na^{1+} to Ca^{2+} pushed the Eu^{3+}/Eu^{2+} redox couple to an even more cathodic potential (Figure 2, top pane, blue trace). The precise reduction potential of Eu^{3+} in $CaCl_2$ could not be determined because the redox wave lay on top of the Cl^{1-}/Cl_2 oxidation wave. In this case, very little reduction current ($Eu^{3+} \rightarrow Eu^{2+}$) passed in the voltammogram in $CaCl_2$, presumably because nearly all of the Eu^{3+} in solution had been reduced by Cl^{1-}. The oxidation current ($Eu^{2+} \rightarrow Eu^{3+}$), however, was clearly much larger than the background (see the Supporting Information for the background voltammograms of each salt matrix). Notice that these results were qualitatively consistent with the aforementioned Eu L_3-edge XANES data.

Many characteristics from the Eu^{3+}/Eu^{2+} electron transfer processes described above were shared by $YbCl_3$ and $SmCl_3$ in molten $CaCl_2$, NaCl, and KCl at 850 °C (Figure 2, Table 2). For instance, quasi-reversible redox waves corresponding to Yb^{3+}/Yb^{2+} and Sm^{3+}/Sm^{2+} redox couples were observed. Important metrics from these voltammograms were captured in Table 2 and compared in Figure 2. In general, moving from Eu to Yb to Sm shifted the reduction potential ($E_{1/2}$) negative, as expected based on the relative standard reduction potentials (E^o) of Eu vs. Yb vs. Sm.[63] Changing the molten salt identity from K^{1+} to Na^{1+} to Ca^{2+} also pushed the redox

potentials positive, which seems to correlate with polarization power (measure of M^{n+} size and charge) of the molten salt cation ($Ca^{2+} > Na^{1+} > K^{1+}$). The most polarizing cation (Ca^{2+}) made the $Ln^{3+} + e^{1-} \rightarrow Ln^{2+}$ redox reaction most accessible. Note, insolubility of $YbCl_3$ in $CaCl_2$ at 850 °C prohibited obtaining a voltammogram of $YbCl_3$ in this matrix. It is also important to point out that unlike the Eu^{3+}/Eu^{2+} couple, the Yb^{3+}/Yb^{2+} and Sm^{3+}/Sm^{2+} reduction potentials lie far negative of the oxidation edge of the solvent window (where Cl^{1-} oxidation to Cl_2 occurs, about +1 V). The more negative potentials protected Yb^{3+} and Sm^{3+} from reduction by Cl^{1-} under our experimental conditions.

Scan rate dependent cyclic voltammograms have been provided in the Supporting Information. Sigmoidal line shapes were observed at slow scan rates, likely owing to convection effects from a temperature gradient within the molten salt. Contributing factors to temperature variation – and in turn convection – were associated with placement of the heating elements, the thermocouples' contact at outer walls of the electrochemical cell, and the electrodes (which provided a heat sink because they extended from the molten salt solution to the top of the furnace).

First-Principles Molecular Dynamics (FPMD) Simulations. The calculated Eu^{3+}/Eu^{2+} redox potentials were consistent with the cyclic voltammetry and XANES results described above. These potentials were calculated with respect to a Ag/AgCl reference in the molten salts of KCl, NaCl, and $CaCl_2$ (Table 3). The computational results did an excellent job reproducing the overall trend observed experimentally; although, there was not an exact one-to-one match in the calculated and experimental $E_{1/2}$ values. For example, the calculations showed the Eu^{3+}/Eu^{2+} reduction potential shifted positive by 0.19 V when the molten salt identity changed from KCl to

NaCl. This theory result corresponded well with the 0.12 V shift observed experimentally. Similarly, changing from KCl to $CaCl_2$ pushed the calculated reduction potential positive by 0.93 V, which also agreed well the experimental measurement that showed a shift of >0.5 V.

Also included in Table 3 is a summary showing how Bader charges for a Eu^{3+} cation surrounded by six Cl^{1-} ligands in the first coordination sphere changed as a function of outer-sphere molten salt cation identity, namely K^{1+}, Na^{1+}, and Ca^{2+}. For example, the Bader charges for Eu^{3+} with outer-sphere K^{1+} and Na^{1+} cations were calculated to be indistinguishable when the uncertainty in the values were considered, at -2.97 ± 0.09 and -2.96 ± 0.10, respectively. These Bader charges were very close to the predicted formal charge of -3, as predicted for a cluster containing one Eu^{3+} trication and six Cl^{1-} monoanions. In contrast, the Bader charge decreased substantially to -2.78 ± 0.08 when the outer sphere cation was changed to Ca^{2+}. This result indicated that Ca^{2+} (high polarization power) was more effective at removing electron density from Eu^{3+} across the $Eu-Cl\cdots Ca^{2+}$ linkage than the K^{1+} (weak polarization power) and Na^{1+} (intermediate polarization power).

Rate of Eu^{3+} Reduction to Eu^{2+}. Spontaneous reduction of Eu^{3+} to Eu^{2+} was characterized as a function of the molten salt cation identity (Ca^{2+} vs. Na^{1+} vs. K^{1+}) and as a function of time (Figure 3). Within the time resolution of the experiment, Eu^{3+} reduced immediately to Eu^{2+} in $CaCl_2$. For example, ~5 min after adding $EuCl_3$ to the molten $CaCl_2$, the open circuit potential lay negative of the $Eu^{3+/2+}$ reduction peak (at around 0.9 V, Figure 2). Furthermore, very little cathodic current passed when scanning negative from this resting potential. This indicated that nearly all of the Eu^{3+} had reduced to Eu^{2+} upon addition of $EuCl_3$ to the molten salt. Another indicator that reduction occurred rapidly came from the fact that we were unable to observe

appreciable amounts of electrochemically generated Eu^{3+} by cyclic voltammetry. For instance, very little cathodic current was observed when cycling the applied potential rapidly (10 V/s) from negative to positive and then negative again.

The Eu^{3+} cation also reduced to Eu^{2+} in molten NaCl and molten KCl, admittedly at rates that were much slower than observed for $CaCl_2$. Although quantitative evaluation of these rates was not possible using our equipment, qualitatively monitoring the open circuit potential as a function of time showed that heating $EuCl_3$ (1% wt, 850 °C) in NaCl and in KCl resulted in complete conversion to Eu^{2+} within 15 h. Initially, the open circuit potentials in both NaCl (+0.8 V) and KCl (+0.55 V) lay positive of the onset of the Eu^{3+} reduction waves in each salt. Over time the open circuit potentials drifted negative before dropping off sharply and reaching a plateau around −0.4 V. We presume the sharp drop-off occurred when essentially all of the Eu^{3+} converted to Eu^{2+}, thereby reaching an undefined resting potential (i.e. the reaction quotient, Q, in the Nernst Equation was undefined because $[Eu^{3+}] = 0$ M). Figure 3 shows cyclic voltammograms of europium in NaCl and KCl immediately (ca. 5 min) after addition of $EuCl_3$ to the molten salts at 850 °C (blue traces) and after 15 hours at 850 °C (green traces). In the cyclic voltammograms taken after 15 hours of heating, the starting potential (which was the open circuit potential, indicated by black arrows in Figure 3) lay negative of the reduction peak. Furthermore, essentially no cathodic current was observed in the first cycle of these cyclic voltammograms, but after cycling positive, a reduction peak appeared, due to generation of Eu^{3+} during the measurement.

We proposed that the reduction of Eu^{3+} reaches completion in all three molten salts because the electrochemical cell is an open system. In other words, as Cl_2 was generated it could diffuse

from the molten salt solution as a gas. We assume this pushed the $Eu^{3+} + Cl^{1-} \rightarrow Eu^{2+} + \frac{1}{2} Cl_2$ reaction toward product formation.

There were some differences between the electrochemical experiments and the XANES experiments described above. We proposed that this may be due in part to factors like convection and lack of stirring throughout the experiment. The most obvious difference was the degree to which Eu^{2+} was generated during heating in molten salts. For example, samples prepared for XANES measurements produced only about 50% reduction of Eu^{3+} to Eu^{2+} after 12 hours of heating at 850 ℃ in NaCl and negligible reduction in KCl under these same conditions. In contrast, the europium in the samples prepared for electrochemical experiments reduced completely to Eu^{2+} in about the same time frame at the same temperature. Differences in Eu^{2+} formation during the XANES vs the electrochemical experiments were likely related to differing concentrations of lanthanide, the europium content in the XANES experiments being ten times larger than in the electrochemical experiments. Hence, it required longer reaction time to reduce the larger quantity of europium. Similar concentration effects may also be responsible for color differences that were observed. For example, heating $EuCl_3$ (1% wt.) for 15 h in NaCl and monitoring the sample by potentiometric methods generated a final product that was white in color, not purple as observed in the more concentrated XANES studies (10% by wt. Eu loading, *vida supra*). Despite difference in color and europium content, the cyclic voltammetry data at 850 ℃ from both sample preparation methods (1% and 10% by wt. Eu loading) were equivalent. Toward this end, we are currently in the process of developing methods for *in situ* XANES and EXAFS measurements that are compatible with the high-temperatures associated with the molten salt matrix and the low energies required for Eu L_3-edge XANES and EXAFS.

Aqueous Voltammetry. The following experiments showed that Eu^{3+}/Eu^{2+} reduction potential

varied with salt cation, even when alkali and alkaline salts were dissolved in more conventional

matrices (like aqueous solutions) and when diluted substantially. Here, these alkali and alkaline

cations served a different role: they were electrolytes, not part of the solvent. All of these

electrolytes were dissolved in water and the electrolyte concentration held at 5 M. To these

solutions, hydrated $EuCl_3 \cdot X H_2O$ was added so that the Eu^{3+} concentration equaled

approximately 5 mM. All aqueous electrochemical measurements were made using a glassy

carbon disk working electrode, graphite rod counter electrode, and a Ag/AgCl (in saturated KCl

solution) reference electrode. All solutions showed a quasi-reversible Eu^{3+}/Eu^{2+} redox process

with reduction potentials near –0.5 V (Figure 4 and Table 4), as expected based on numerous

electrochemical studies on europium.[46,64,65] Similar to the results in molten salts described above,

the Eu^{3+}/Eu^{2+} reduction potential varied as a function of electrolyte identity, albeit to a much

lesser extent (Figure 5). For instance, the same trend toward decreasing potential occurred as the

identity of the supporting electrolyte shifted from having strong to weak polarization power;

$CaCl_2$ to LiCl to NaCl to CsCl. Results were benchmarked against the NMe_4Cl electrolyte, which

contained a NMe_4^{1+} cation often regarded as non-coordinating.[5] Note, KCl was not used for

aqueous studies because its solubility in water only reaches about 4.5 M. Within this series, the

Eu^{3+}/Eu^{2+} reduction potential ($E_{1/2}$) with the soft NMe_4^{1+} cation was furthest negative (–0.64 ±

0.02 V) and with the strongest Lewis acid in our series (Ca^{2+}) was most positive (at –0.49 ± 0.02

V).

Outlook

Electron transfer chemistry accessible to Eu, Yb, and Sm in a series of molten salt matrices ($CaCl_2$, NaCl, KCl) has been characterized using *in situ* electrochemical methods within the melt at 850 ºC, *ex situ* X-ray absorption spectroscopy measurements (made after the samples were cooled to room temperature), and first-principles molecular dynamics simulations. We interpreted the results as suggesting that the outer-coordination sphere molten salt cation substantially impacted the electron transfer event that occurred on the lanthanide. For instance, the Ln L_3-edge XANES data showed that Ln^{3+} reduction was dependent on molten salt cation identity. Reactions with $CaCl_2$ favored formation of Eu^{2+}, reactions with NaCl generated a mixture of Eu^{2+} and Eu^{3+}, and reactions with KCl favored Eu^{3+}. Similarly, the electrochemical data showed that the Eu^{3+}/Eu^{2+}, Yb^{3+}/Yb^{2+}, and Sm^{3+}/Sm^{2+} reduction potentials shifted substantially (ca. 0.5 V) when the molten salt identity changed from $CaCl_2$ to NaCl to KCl. Reduction potentials were between +1.0 and +0.55 V for europium, −0.18 and −0.31 V for ytterbium (excluding in $CaCl_2$), and −0.15 to −0.61 V for samarium. The computational results on europium reproduced the overall behavior observed experimentally, showing that Eu^{3+}/Eu^{2+} reduction potentials shifted positive systematically as a function of the molten salt cation identity from K^{1+} to Na^{1+} to Ca^{2+}. Characterizing the Eu^{3+}/Eu^{2+} electron transfer process using electrochemistry showed that $EuCl_3$ (1% by wt., 850 °C) spontaneously and instantaneously reduced to Eu^{2+} in $CaCl_2$ solutions and that stability of Eu^{3+} was not persistent in NaCl and KCl. For example, monitoring the open circuit potential during prolonged heating of $EuCl_3$ (>12 h) under these conditions showed that Eu^{3+} reduced slowly and entirely to Eu^{2+} in both NaCl and KCl. This indicated that the reduction of Eu^{3+} by Cl^{1-} occurred spontaneously in each of the three salts under these experimental conditions.

We rationalized these observations in the following way. Based on solid-state structures, we inferred that lanthanide inner-coordination environments were best described as being saturated with Cl^{1-} in a molten salt.[66] The molten salt cations, in turn, were in the outer-coordination spheres and available to interact with the Ln cations across the lanthanide–chloride bridges, e.g. $Ln–Cl\cdots M^{n+}$ (Ln = Eu, Yb, Sm; M^{n+} = Ca^{2+}, Na^{1+}, K^{1+}; Scheme 1). This interpretation was corroborated by computational modeling and experimental EXAFS data, which is the subject of a subsequent publication. We speculated that highly charged, small cations, with substantial polarization power (like Ca^{2+}), inductively removed electron density from the lanthanide cations. Under these conditions the Ln^{3+}/Ln^{2+} reduction potential shifted positive and formation of electron-rich and low-oxidation state species (like Eu^{2+}, Yb^{2+}, and Sm^{2+}) was accelerated. Conversely, cations with weak polarization power (low charge and large ionic radius), like K^{1+}, were less effective at removing electron density from the lanthanide ions. These weakly polarizing cations lowered the Ln^{3+}/Ln^{2+} reduction potentials and slowed formation of Ln^{2+}. This interpretation was supported by the calculated Bader charges, which demonstrate that Ca^{2+} inductively removes electron density from Eu^{3+} to a larger extent than that of K^{1+} and Na^{1+}.

Comparing the Eu^{3+}/Eu^{2+} electrochemical data in molten salts to those in aqueous solutions provided another example of the profound influence that the outer-coordination sphere can have on lanthanide electron transfer chemistry (Figure 5). Changing the salt cation identity in molten salts (K^{1+} to Na^{1+} to Ca^{2+}) shifted the Eu^{3+}/Eu^{2+} reduction potential by over 0.5 V. In contrast, in aqueous media the Eu^{3+}/Eu^{2+} redox couple was only mildly impacted by the identity of the supporting electrolyte cation. Changing the outer-coordination sphere cation from NMe_4^{1+} to Cs^{1+}, Na^{1+}, Li^{1+}, and Ca^{2+} only shifted the Eu^{3+}/Eu^{2+} reduction potential by around 0.15 V (i.e. 1/3 of the impact in molten salt solutions). We attributed this attenuation of cation impact on the

Eu^{3+}/Eu^{2+} redox couple in aqueous media to water disrupting occupancy of the secondary coordination sphere. In aqueous solutions, it is well established that water and chloride compete with the M^{n+} cation for occupancy of this secondary coordination sphere. In this scenario, the M^{n+} cation can be pushed from the secondary sphere ($Eu–Cl\cdots M^{n+}\cdots H_2O$ and $Eu–H_2O\cdots M^{n+}\cdots Cl$) to the tertiary sphere ($Eu–Cl\cdots H_2O\cdots M^{n+}$ and $Eu–H_2O\cdots Cl\cdots M^{n+}$).[67,68] Inductive effects from the M^{n+} outer-sphere cation on the central europium metal weaken when the M^{n+} is expelled to the tertiary coordination sphere because of the longer $Eu\cdots\cdots M^{n+}$ distances. In contrast, when water was not present (in the molten salts), the primary coordination sphere was saturated with Cl^{1-} ions and M^{n+} occupancy in the secondary coordination sphere increased. Because of this, the M^{n+} cation's impact on the Ln^{3+}/Ln^{2+} reduction potential approximately tripled. We inferred that inductive influence from the outer-coordination sphere M^{n+} cation on the Eu^{3+}/Eu^{2+} redox event was strengthened at these shorter $Eu\cdots M^{n+}$ distances.

Taken as a whole, these results highlight how assumptions based solely on traditional measurements made in aqueous solutions and organic solvents limit understanding of the electron transfer reactions. For instance, the Eu^{3+}/Eu^{2+} reduction potential is not confined between -0.49 ± 0.02 V and -0.64 ± 0.02 V, as one would conclude if only aqueous measurements were considered.[46,64,65] This electron transfer reaction is instead quite dynamic. It can be pushed as far positive as $+1.0$ V in molten salts. We attribute a large portion of this shift to the impact of the outer-coordination sphere cation and acknowledge influences from other variables, e.g. the number of inner-sphere Cl^{1-} (vs. H_2O) ligands, temperature, etc. From this perspective, the molten salt framework provides an exceptional testbed for expanding understanding of outer-coordination sphere impact on redox transformations and provides opportunity to quantify those effects using cyclic voltammetry. Our current efforts are centered

on expanding to other molten salt systems (for both transition metals, other 4*f*-systems, and 5*f*-block elements), which we believe will provide the versatility and tunability needed to systematically define many aspects of outer-coordination sphere influence on chemical and electrochemical transformations. If successful, these types of studies may open doors to more fully exploit electron transfer reactions for technological advancement. We hope that the results described here will stimulate thought, insight, and research efforts to develop better understanding of outer-coordination sphere impact, so that redox transformations can be controlled with more fidelity and purpose.

Methods

General Consideration. Potassium chloride (KCl, 99.99%, anhydrous beads, Millipore Sigma), sodium chloride (NaCl, 99.99%, anhydrous beads, Millipore Sigma), cesium chloride (CsCl, 99.999%, FisherBiotech), lithium chloride (LiCl, 99.98%, Sigma Aldrich) calcium dichloride ($CaCl_2$, 99.9%, anhydrous beads, BeanTown Chemical), silver(I) chloride (AgCl, 99.995%, BeanTown Chemical), europium(III) trichloride ($EuCl_3$, 99.99%, anhydrous powder, Millipore Sigma), samarium(III) trichloride ($SmCl_3$, 99.9%, anhydrous, Alfa Aesar), ytterbium(III) trichloride ($YbCl_3$, 99.9%, Strem), boron nitride (BN, Fisher), and tetramethylammonium chloride (NMe_4Cl, 99.0%, Sigma Aldrich) were obtained commercially and used as received. All water used in these experiments was deionized and passed through a Barnstead water purification system until a resistivity of 18 MΩ was achieved. CH Instruments 620C potentiostat was used for all voltammetric measurements. Success in all experiments in molten salts relied on rigorous exclusion of moisture, air, and volatile organic compounds from the glovebox atmosphere. Hence, crucibles were fired prior to use; the $CaCl_2$, NaCl, KCl, $EuCl_3$, and $SmCl_3$

salts were obtained in anhydrous form, in sealed ampules, and stored in the glovebox; and all electrochemical setup components were dried in an oven at 200 °C before use. The glovebox had to be rigorously free of organic solvents, through removal of all solvent bottles and thorough atmosphere recycling. Omission of any of these details caused deleterious side reactions that generated black solids, which were difficult to characterize.

Europium(III) Trichloride Electrochemistry in Molten Salt Matrices. All voltammetric measurements made in molten salt matrices were conducted in an argon filled glovebox with rigorous exclusion of air, moisture, and organic solvents. Experiments utilized a custom-made vertical furnace (ThermCraft RH211; 6 in. tall) and had alumina based ceramic fiber insulation (3-1/8 in. thickness) that covered two 180° semi-cylindrical ceramic heating elements (2 in. tall, 1.25 in. inner diameter, 100 W, 28.5 V). These heating elements were arranged around a central hole (diameter 1.25 in.; Figure S1) and enclosed in a manufacturer supplied insulation package. The hole was bored through the top of the apparatus ending approximately 2 in. above the bottom of the insulation. A steel tube (outer diameter = 3.1 cm, length = 10 cm) was inserted into this hole to act as a liner within the furnace and hold an electrochemical cell in place in the center of the heating elements. Power was supplied by a Meanwell 27V DC power supply (ESP-240-27) and controlled by an Omega PID controller (CN8DPT-440-DC) through a Crydom 100VDC/60A solid-state relay (D1D60). Overtemperature protection was provided by an Omega limit switch (CN708) connected to an independent thermocouple probe. The electrochemical cell was a quartz test tube (2.7 cm outer diameter, 13.5 cm tall, 0.1 cm wall thickness). Photographs of the furnace are provided in the Supporting Information.

Electrochemical measurements relied on glassy carbon rod working and counter electrodes (3 mm diameter, Alfa Aesar) that were cleaned and polished with a felt polishing pad and a slurry of alumina powder (0.05 μm) in water. The electrochemical measurements were referenced using a silver wire (0.1 cm diameter, 99.999%, BeanTown Chemical) that was encased in a mullite tube (5 mm outer diameter, 1 mm wall thickness, 14 cm tall, Anderman Industrial Ceramics). The tube contained an intimate mixture of AgCl (0.5 mg, 1% by weight) and alkali or alkaline salt (KCl, NaCl, or $CaCl_2$; 50 mg) that was ground with a mortar and pestle prior to use. A fresh reference electrode (new salt, clean Ag wire, clean mullite tube) was assembled for each experiment to minimize cross-contamination. (The Ag wire was cleaned with coarse steel wool and rinsed with water. The mullite tube was rinsed with water and soaked (inside and outside) in concentrated HCl, then rinsed with water again.) The electrochemical cell was charged with solid alkali or alkaline earth metal chloride salts (NaCl, KCl, $CaCl_2$; 2.5 g) and then loaded into the furnace. The electrodes were inserted in the cell and held approximately 1.3 cm apart. Care was taken to ensure that the electrode tips extended to nearly equivalent depths within the salt. All electrochemical equipment (electrodes, mullite tube, and electrochemical cell) were dried in an oven (200˚C) before entry into the glovebox. *¡Notice! Drying this equipment is critical, otherwise a black decomposition product will form in the molten salt mixture after addition of europium.*

The furnace was operated using an Omega PID controller (CN8DPT-440-DC) equipped with an Omega limit switch (CN708) and a Crydom 100VDC/60A solid-state relay (D1D60). This electronic apparatus was connected to two thermocouple probes (one for the controller and one for the limit switch) that were positioned to monitor temperature between the steel tube and the quartz electrochemical cell. The furnace was heated (as fast as possible, full power) and held at

the desired temperature (850˚C) until the reference electrode reached a stable potential. Monitoring the open circuit potential of the cell revealed that stability was typically reached in 2 h (which is consistent with existing literature on molten salt reference electrodes.[56,57] After characterizing the reduction and oxidation potentials for the molten salt and confirming that no electron transfer processes occurred between those potentials, the appropriate $LnCl_3$ (25 mg; 1% $LnCl_3$ by weight) was dropped into the cell using a plastic weigh boat. Homogeneity was achieved by stirring the solution with the electrodes for about 10 seconds. Each set of data was reproduced in triplicate.

Europium(III) Trichloride Electrochemistry in Aqueous Matrices. In a hood, a three-electrode cell was used, consisting of a glassy carbon disk working electrode (0.3 cm diameter), a graphite rod counter electrode, and a fritted Ag/AgCl (saturated KCl) reference electrode. All of these electrodes were purchased from CH Instruments and the working electrode was cleaned and polished on a felt polishing pad with alumina powder (0.05 μm) suspended in water. The cell consisted of a glass cylindrical body and a PTFE cap with holes to hold the electrodes in place. A small section of PTFE tubing (22 gauge) was inserted through a small hole in the PTFE cap and used to flow argon into the cell. Electrolyte stock solutions (LiCl, NaCl, CsCl, $CaCl_2$, and NMe_4Cl) were prepared by dissolving the electrolyte salt in water to reach electrolyte concentrations of 5 M (10 mL volume). Each of these resulting solutions were kept as stock solutions and used to collect replicate trials of voltammetry. For the voltammetric measurements, one of these prepared electrolyte solutions was selected and transferred (2 mL) to the electrochemical cell and de-aerated with argon for 5 minutes prior to conducting measurements. Argon was continuously flowed through the cell headspace during voltammetric data acquisition.

After characterizing the potential windows for the aqueous electrolyte solutions and confirming that no electron transfer processes occurred within that window, $EuCl_3$ (2.5 mg, 0.01 mmol; 5 mM) was added. Homogeneity was achieved by sparging the solution (5 min) between measurements. Cyclic voltammograms were collected. Each data set was collected in triplicate by making measurements on subsequent days, using 2 mL aliquots of the electrolyte stock solutions (5 M in electrolyte).

XANES Sample Preparation. Anhydrous europium, ytterbium, and samarium chlorides ($EuCl_3$, $EuCl_2$, $YbCl_3$, and $SmCl_3$) and mixtures of europium, ytterbium, and samarium trichloride ($EuCl_3$ and $SmCl_3$) in alkali and alkaline earth chloride salts were heated at high temperatures (1 °C/min to 850 °C and held at 850 °C for 12 h) in a muffle furnace located within an Ar atmosphere dry box. The mixtures were achieved by combining $LnCl_3$ (10 wt%, Ln = Eu, Yb, or Sm) in anhydrous MCl_n (M = Na, K, or Ca) and grinding via mortar and pestle. The powder was then transferred to an open Al_2O_3 crucible prior to the high temperature firing. After the salt mixture returned to room temperature, the salt puck was extracted by crushing the crucible with a hammer. Judicious effort was undertaken to ensure clean cleavage of the crucible and the subsequent removal of any alumina pieces. These samples were then doubly sealed under Ar and shipped to the Stanford Synchrotron Radiation Lightsource (SSRL). Fluorescent measurements with a 100-element Ge-detector were conducted at 10 K in single slot aluminum sample holders (3 mm × 30 mm). Specifically, the lanthanide halide mixture was contained within two Kapton-tape windows (37 μm thick). Optimal fluorescence was achieved by diluting the salt mixture with anhydrous BN to ensure homogeneous sample configuration.

XANES Data Acquisition. The XANES data were collected at SSRL under dedicated operating

conditions (3.0 GeV, 5%, 500 mA) on end station 11-2. This beamline was equipped with a 26-

pole, 2.0 tesla wiggler. Using a liquid nitrogen-cooled double-crystal Si(220) ($\Phi = 0^{\circ}$)

monochromator and employing collimating mirrors, a single energy was selected from the

incident white beam. Vertical acceptance was controlled by slits positioned before the

monochromator. All measurements were conducted with the monochromator crystals fully-

tuned. For these experiments, higher harmonics from the monochromatic light were removed

using a 370 mm Rh coated harmonic rejection mirror. The Rh coating was 50 nm with 20 nm

seed coating on a Zerodur substrate. The harmonic rejection cut-off was set at 11000 eV by the

mirror angle, thereby controlling which photons experience total external reflection.

The samples were attached to the beamline 11-2 XANES rail. The rail was equipped with

three ionization chambers through which nitrogen gas was continually flowed. One chamber (10

cm long) was positioned before the sample holder, to monitor the incident radiation (I_0). The

second chamber (30 cm long) was positioned after the sample holder, such that sample

transmission (I_1) could be evaluated against I_0, while a third chamber (I_2, 30 cm long) was

positioned downstream from I_1 so that the XANES of a calibration foil could be measured *in situ*

during the XANES experiments against I_1. All lanthanide L_3-edge XANES samples were measured by monitoring sample fluorescence against the incident radiation (I_0). An additional 100 element Ge fluorescence detector was positioned at 90° to the incident radiation (I_0) and windowed on either the Eu Lα_1-emission line (5,846 eV), Yb Lα_1-emission line (7,416 eV) or the Sm Lα_1-emission line (5,637 eV). With this designation, lanthanide L_3-edge XANES spectra were recorded in fluorescence mode as the ratio of fluorescence intensity over the intensity of the incident radiation (I_0). High-energy contributions to the fluorescence signal were removed by equipping the Ge detector with Soller slits and either a Cr filter (3 absorption lengths; for Eu) or no filter (for Sm and Yb).

XANES Data Analysis. Data manipulations and analyses were conducted as previously described.[69,70] The Eu L_3-edge spectra were calibrated to Co (7,709.0 eV), the Yb L_3-edge spectra were calibrated to Ni (8333 eV), and the Sm L_3-edge spectra were calibrated to Mn (6,539.0 eV). All calibration samples were measured *in situ*. To correct for detector dead time, nonlinear response curves were defined from 0 to ~70% dead time (windowed counts of the emission line versus the total incoming counts into the solid-state detector) using a Cr 3-mm filter (~400 above the Cr K-edge). Each channel was manually surveyed for outliers, which were

omitted. The deadtime correction was applied before averaging the individual channels. Then,

the 8 individual scans were aligned with the *in situ* calibration foil and averaged using IFEFFIT[71]

within the Athena software package. The XANES data were analyzed by fitting a line to the pre-

edge region, which removed the background from experimental data in the spectra. Then a third

order polynomial fit was chosen for the post-edge region. The difference between pre- and post-

edge lines was set to unity at the first inflection point, normalizing the absorption jump to 1.0.

To remove contributions from low frequency noise, a spline function was fit over the absorption

background of an isolated atom and subtracted from the data.

Computational Details. Combining density functional theory (DFT) calculations and implicit

solvation models[72] to predict the redox potential for molecular systems dissolved in ordinary

liquids[73] or room temperature ionic liquids[74] has become a standard protocol in the past

decades.[75,76] However, this approach is difficult to directly apply in the calculation of molten

salts due to the lack of the proper implicit models representing the strong participation of the

solvent medium on the electronic structure of the solute. Therefore, in this study we carried out

FPMD simulations using the Vienna *ab initio* simulation package (VASP)[77,78] based on DFT and

the Born-Oppenheimer approximation with periodic boundary conditions to account for the

molten salt solvents explicitly. The simulation supercells contained 1 Eu atom and 32 cations (K

or Na or Ca) and the corresponding numbers of Cl atoms to model the charge neutral simulation

cell KCl−EuCl$_n$, NaCl−EuCl$_n$, and CaCl$_2$−EuCl$_n$ (n=2, 3) mixtures at 3 mol% europium

concentration. The cubic simulation cell length varied from 14.21 Å (KCl), 13.07 Å (NaCl), and

14.43 Å (CaCl$_2$) to approximate the isometric mixing of the experimental density of each salt at

1100 K.

The interaction among the electrons and the nucleus was described by the projector

augmented wave (PAW) method,[79,80] and the Perdew-Burke-Ernzerhof (PBE) functional of the

generalized gradient approximation (GGA) was used for the electron exchange-correlation.[81]

Standard PAW-PBE pseudopotentials were used for Na ($3s^1$), K_pv ($3p^64s^1$), Ca_sv ($3s^23p^64s^2$),

(Cl ($3s^23p^5$), and Eu ($5s^25p^66s^24f^7$), with the energy cutoff of 420 eV for the plane wave basis

set. The Brillouin zone was sampled with the Γ-point only. Dispersion forces were included with

the DFT-D3 Hamiltonian.[82] Spin polarization was applied to allow for the open-shell nature of

the Eu^{2+} and Eu^{3+} ions, that have seven and six unpaired electrons, respectively.

FPMD simulations were carried out in the NVT canonical ensemble using a Nosé-

thermostat[83,84] corresponding to a period of ~80 fs with the time step of 4 fs. The simulation

temperature was set at 1100 K. As illustrated in Scheme 2, the redox potentials for Eu(III)/Eu(II)

were calculated with Cl$_2$/Cl$^-$ reference,[85]

$$\langle V_{redox} \rangle_{EuCl_3/EuCl_2}\left(vs.\ Cl_2/Cl^-\right) = -\frac{\Delta A}{nF} =$$
$$-\frac{\left[\langle E(EuCl_2 + MS)\rangle + 0.5 \cdot G(Cl_2) - \langle E(EuCl_3 + MS)\rangle\right] + C^S}{1 \cdot e}$$

in which MS denotes the molten salt, $<E>$ the ensemble average of the total energy calculated from FPMD production, F the Faraday constant, e the absolute value of the electron charge, G (Cl_2) the free energy of chlorine gas at the temperature of the calculation and one atmospheric pressure, and C^S the entropy correction term. The total simulation time to calculate $<E>$ was about 80 ps, after the equilibration of 20 ps for each mixture. The starting structures for Eu(II) systems before equilibration were taken from their Eu(III) counterparts by removing one Cl atom in the simulation box. The reported redox potential of Ag/AgCl with respect to Cl_2/Cl^- (-1.1293 V) in molten salts was used to shift the redox potential for the Eu(III)/Eu(II) couple to compare with our experimental measurement.[59] 100 snapshots for each mixture were further selected with the interval of 800 fs to obtain the average charges on Eu solute and the first coordination Cl^{1-} ions with the help of Bader charge analysis.[86]

Conflict of Interest. There are no conflicts of interest to declare.

Supporting Information

Supporting information includes additional cyclic voltammetry data as well as a description of the furnace used for high temperature electrochemical measurements.

Acknowledgments

Figures

Figure 1. Background-subtracted and normalized Ln (Eu, top; Yb, middle; Sm, bottom) L_3-edge X-ray absorption near edge spectroscopy (XANES) data from reaction products that formed after dissolving $LnCl_3$ in molten salts ($CaCl_2$, NaCl, and KCl) at 850 °C. Note measurements were made at room temperature, <u>not</u> *in situ* at 850 °C. Instead, samples were cooled from 850 °C to room temperature and then XANES data collected at 77 K. The legend refers to the reagent mixture compositions <u>*before*</u> heating and the spectra were obtained on the products <u>*after*</u> heating. Zero on the x-axis corresponds to the inflection point from the $LnCl_3$ standard.
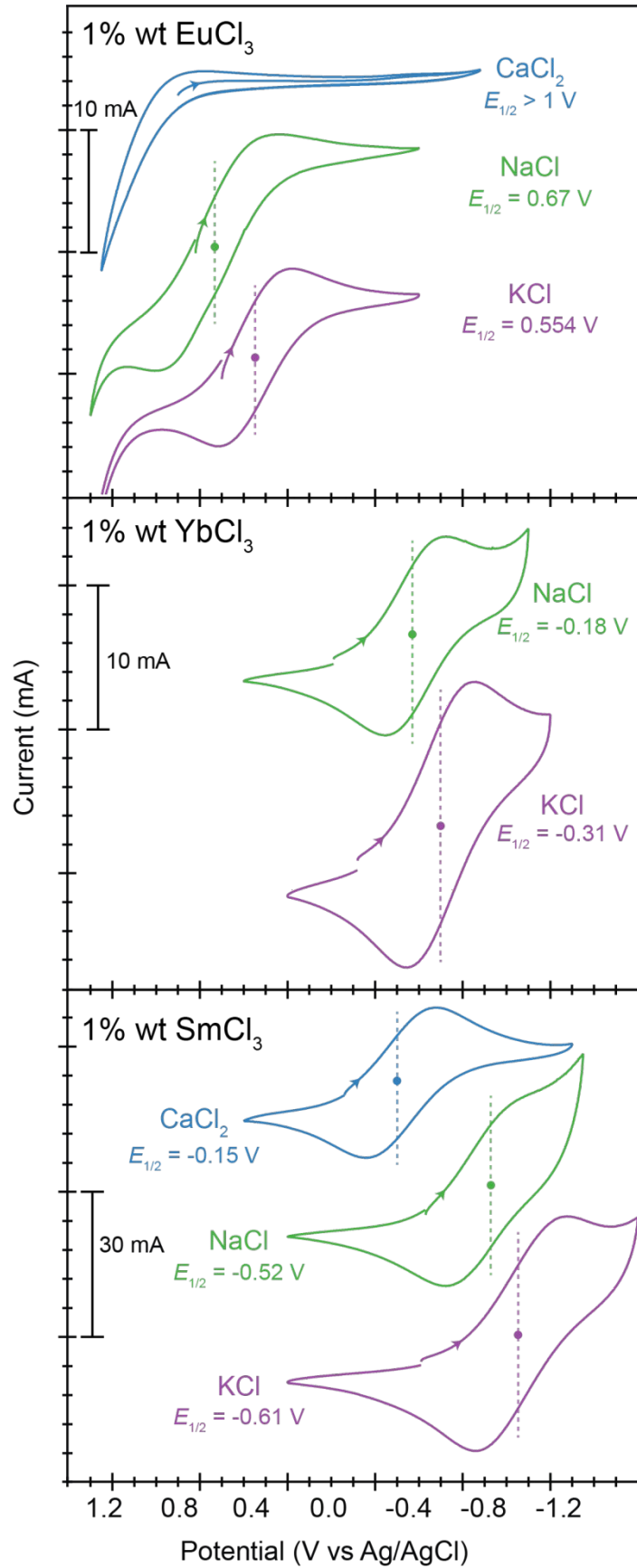
Figure 2. Cyclic voltammograms from solutions that contained $LnCl_3$ [1% wt.; Ln = Eu (*top*), Yb (*middle*), and Sm (*bottom*)] dissolved in molten salts ($CaCl_2$, blue trace; NaCl, green trace; KCl, purple trace) at 850 °C. The voltammogram of $YbCl_3$ in $CaCl_2$ was not included because of $YbCl_3$ insolubility in $CaCl_2$. The dashed vertical lines and solid circles indicate the positions of the reduction potentials ($E_{1/2}$) for the Ln^{3+}/Ln^{2+} redox events, which are also listed in the corresponding color on the plot. Arrows show the scanning direction. Working and counter electrodes were glassy carbon rods. The reference electrode was a silver wire immersed in a solution of AgCl (1% wt.) in the corresponding molten salt and was encased in a mullite tube. All voltammograms were collected at 1 V/s.
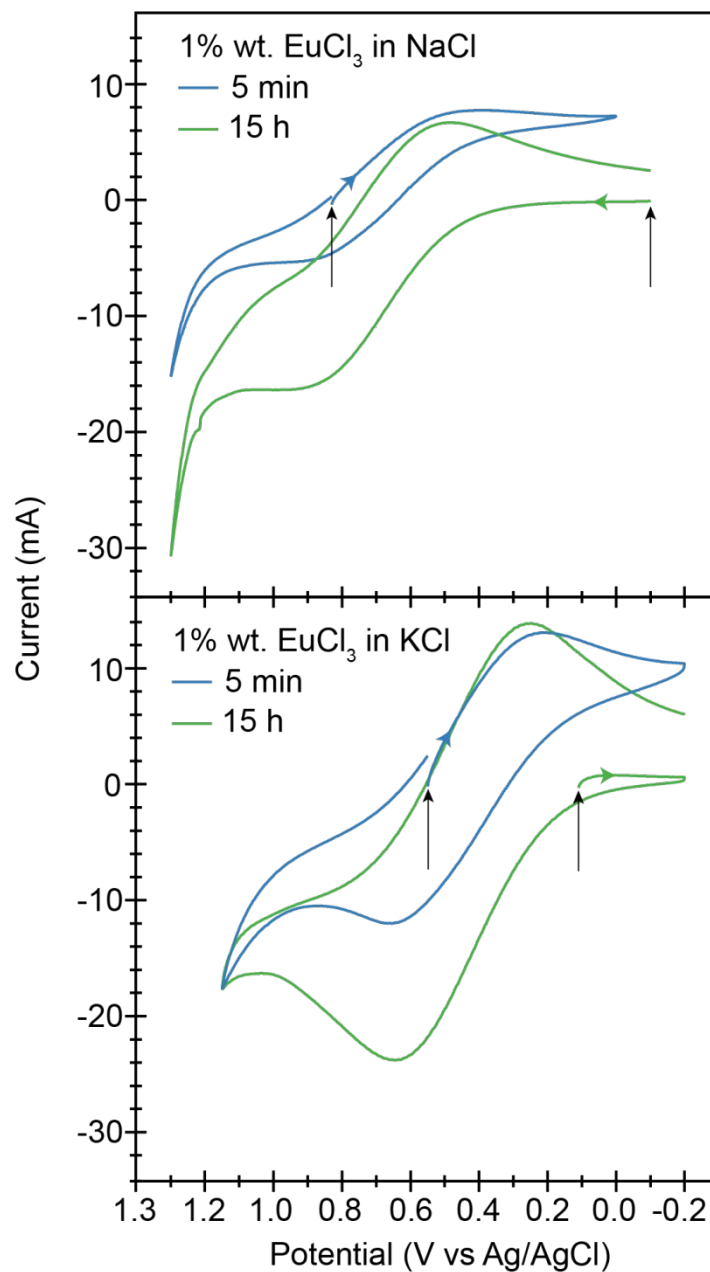
Figure 3. Cyclic voltammograms collected from solutions of EuCl$_3$ (1% wt) dissolved in molten salts (NaCl, *top*; KCl, *bottom*) at 850 °C. The blue trace was collected after holding at 850 °C for approximately 5 min and the green trace was collected after holding at 850 °C overnight. Working and counter electrodes were glassy carbon rods. Colored arrows on the traces show the scanning direction. The black arrows indicate

the starting potential (open circuit potential). The reference electrode was a silver wire

immersed in a solution of AgCl (1% wt.) in the corresponding molten salt and was

encased in a mullite tube. All voltammograms were collected at 1 V/s.
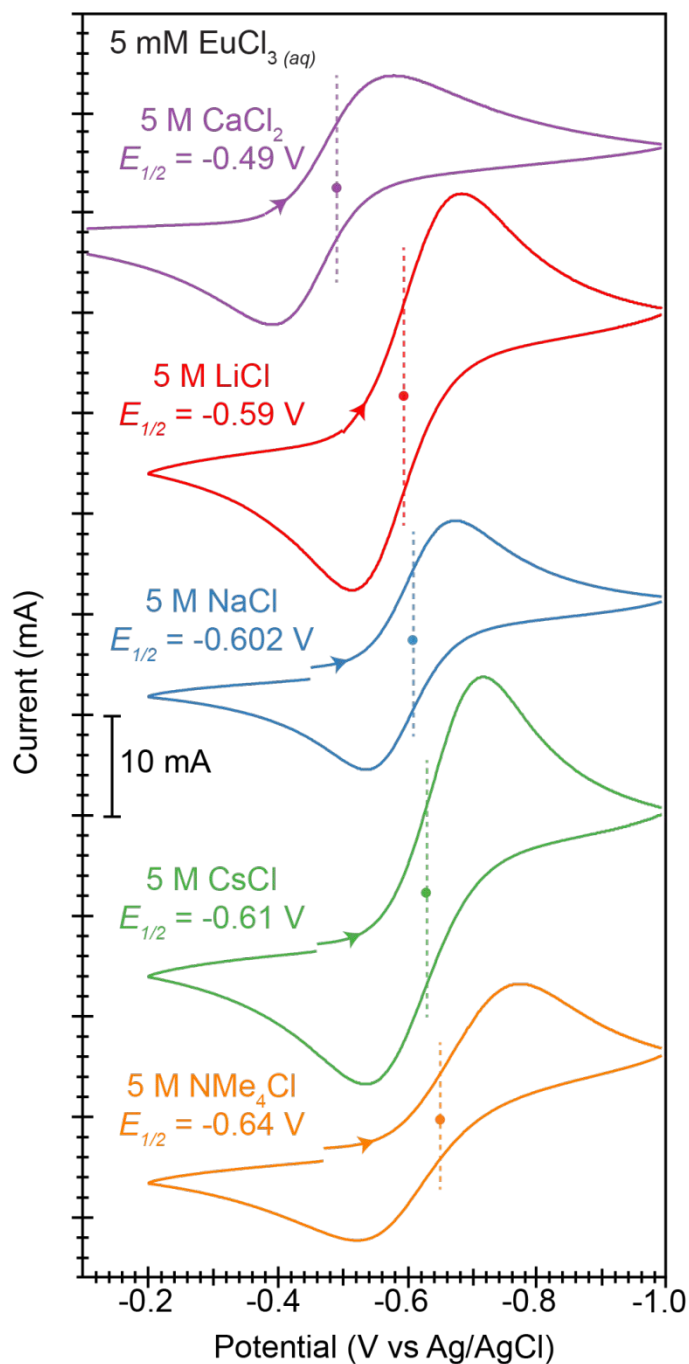
Figure 4. Cyclic voltammograms collected at room temperature from $EuCl_3$ (5 mM) dissolved in aqueous solutions that contained a variety of supporting electrolytes (5 M): $CaCl_2$ (purple trace), LiCl (red trace), NaCl (blue trace), CsCl (green trace), and NMe_4Cl

(orange trace). The dashed vertical lines and solid circles indicate the positions of the reduction potentials ($E_{1/2}$) for the Ln^{3+}/Ln^{2+} redox events, which are also listed in the corresponding color on the plot. The working electrode was a glassy carbon disk (3 mm diameter), the counter electrode was a graphite rod, and the reference electrode was an aqueous Ag/AgCl electrode (in saturated KCl solution). All voltammograms were collected at 50 mV/s.
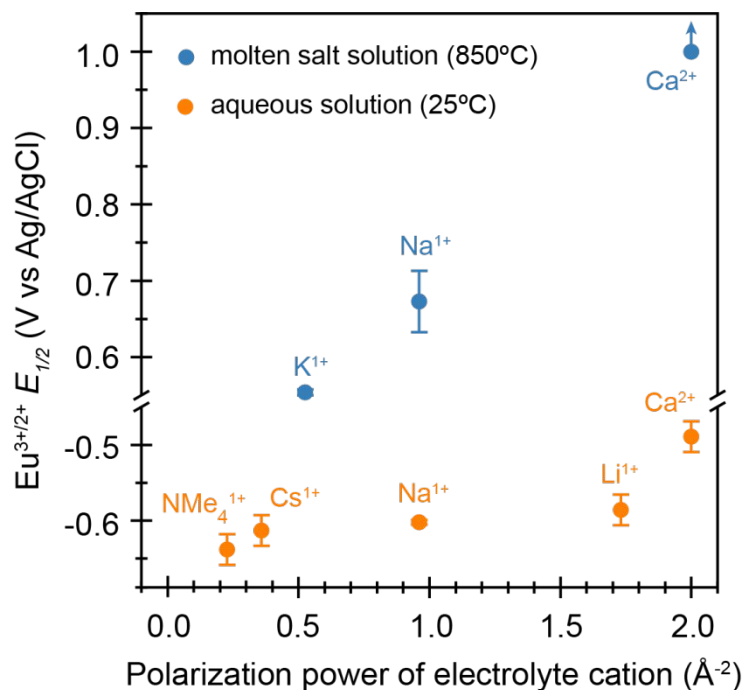
Figure 5. The reduction potentials ($E_{1/2}$) of Eu^{2+}/Eu^{3+} in room temperature aqueous solutions (orange) and in high temperature molten salt solutions (blue) plotted as a function of the electrolyte cation's polarization power [oxidation state ÷ (ionic radius)^2].[87]. The arrow on the blue data point labeled "Ca^{2+}" indicates that the true value is somewhere greater than where the data point is shown.

Tables

Table 1. Inflection points and peak maxima for Ln (Eu, Yb, and Sm) L_3-edge X-ray absorption near edge spectroscopy (XANES) data from reaction products that formed after dissolving $LnCl_3$ in molten salts ($CaCl_2$, NaCl, and KCl) at 850 °C. Note, measurements were not made *in situ* at 850 °C. Instead, samples were cooled from 850 °C to room temperature and then XANES data was collected at 77 K.

Analyte + Molten Salt	Inflection Point (eV)	Ln^{II} Peak Maximum (eV)	Ln^{III} Peak Maximum (eV)
$EuCl_2$	6,973.7	6,967.8	–
$EuCl_3$ + $CaCl_2$	6,973.6	6,975.7	6,982.1
$EuCl_3$ + NaCl	6,974.3	6,975.3	6,983.6
$EuCl_3$ + KCl	6,974.1	6,976.2	6,983.9
$EuCl_3$	6,981.5	–	6,983.7
$YbCl_3$ + $CaCl_2$	8,947.3	8,940.5	8,950.1
$YbCl_3$ + NaCl	8,947.0	–	8,950.1
$YbCl_3$ + KCl	8,946.7	–	8,950.6
$YbCl_3$	8,947.6	–	8,950.3
$SmCl_3$ + $CaCl_2$	6,721.0	6,714.0	6,722.6
$SmCl_3$ + NaCl	6,720.8	–	6,722.6
$SmCl_3$+ KCl	6,720.6	–	6,722.5
$SmCl_3$	6,721.1	–	6,722.9

40

Table 2. The reduction potential ($E_{1/2}$) and the separation between the two peak potentials (ΔE_p) from Ln^{3+}/Ln^{2+} redox couples in molten salts ($CaCl_2$, NaCl, and KCl) at 850°C. Working and counter electrodes were glassy carbon rods. The reference electrode was a silver wire immersed in a solution of AgCl (1% wt.) in the corresponding molten salt and was encased in a mullite tube. All voltammograms were collected at 1 V/s.

Analyte + Molten Salt	$E_{1/2}$ (V)[a]	ΔE_p (mV)[a]
$EuCl_3$ + $CaCl_2$	--	--
$EuCl_3$ + NaCl	0.67 ± 0.04	620 ± 50
$EuCl_3$ + KCl	0.554 ± 0.004	328 ± 9
$YbCl_3$ + NaCl	-0.18 ± 0.01	300 ± 10
$YbCl_3$ + KCl	-0.31 ± 0.02	330 ± 10
$SmCl_3$ + $CaCl_2$	-0.15 ± 0.01	360 ± 20
$SmCl_3$ + NaCl	-0.52 ± 0.04	310 ± 20
$SmCl_3$ + KCl	-0.61 ± 0.05	360 ± 40

[a] All values averaged over three separate measurements.

Table 3. The calculated reduction potentials ($E_{\frac{1}{2},calc}$) of Eu(III) in the series of molten chloride salts with respect to Ag/AgCl reference and the Bader charge (Δe) on Eu(III) with the six Cl^- in the first coordination shell with the geometry cutoff of 4.0 Å.

Analyte + Electrolyte	$E_{\frac{1}{2},calc}$ (V)	Bader charge
$EuCl_3$ + KCl	-0.45 ± 0.24	-2.97 ± 0.09
$EuCl_3$ + NaCl	-0.26 ± 0.34	-2.96 ± 0.10
$EuCl_3$ + $CaCl_2$	0.48 ± 0.41	-2.78 ± 0.08

Table 4. The reduction potentials ($E_{\frac{1}{2}}$) and the separations between the two peak potentials (ΔE_p) for the Eu^{3+}/Eu^{2+} redox couple obtained at room temperature from $EuCl_3$ (5 mM) dissolved in aqueous solutions that contained a variety of supporting electrolytes (5 M). The working electrode was a glassy carbon disk (3 mm diameter), the counter electrode was a graphite rod, and the reference electrode was an aqueous Ag/AgCl electrode (in saturated KCl solution). All voltammograms were collected at 50 mV/s.

Analyte + Electrolyte	$E_{\frac{1}{2}}$	ΔE_p
	(V)[a]	**(mV)**[a]
$EuCl_3$ + $CaCl_2$	-0.49 ± 0.02	220 ± 70
$EuCl_3$ + LiCl	-0.59 ± 0.02	170 ± 30
$EuCl_3$ + NaCl	-0.602 ± 0.003	120 ± 10
$EuCl_3$ + CsCl	-0.61 ± 0.02	154 ± 20
$EuCl_3$ + NH_4Cl	-0.64 ± 0.02	190 ± 50

[a] All values averaged over three separate measurements.

Schemes
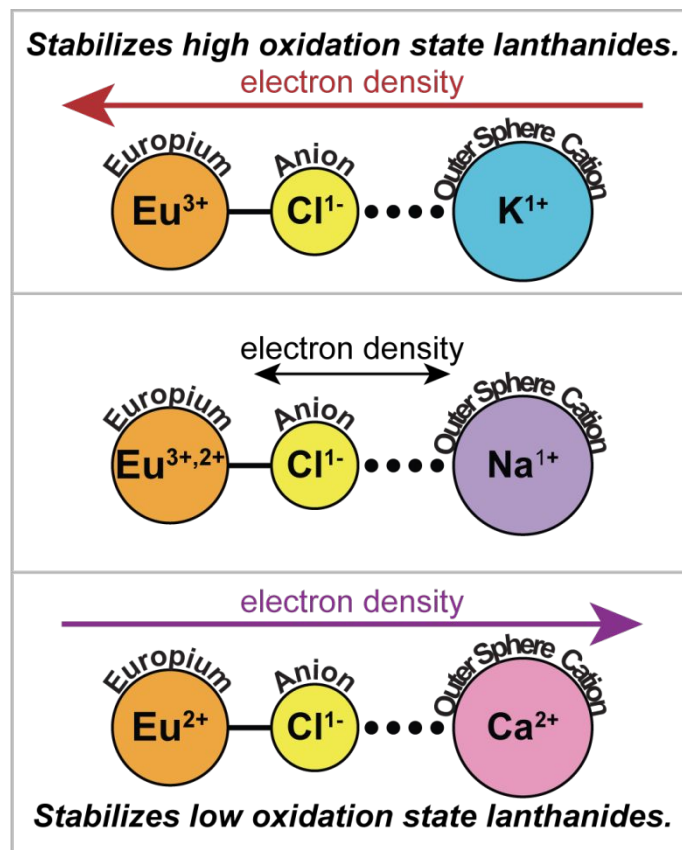
Scheme 1. A cartoon illustrating inductive outer-sphere impacts from molten salt cations (K^{1+}, Na^{1+}, and Ca^{2+}) on lanthanide ions using the Eu^{3+}/Eu^{2+} redox couple as a representative example for other lanthanide cations.

References

(1)   Creutz, S. E.; Peters, J. C. Exploring Secondary-Sphere Interactions in Fe-N_xH_y

Complexes Relevant to N_2 Fixation. *Chem. Sci.* **2017**, *8*, 2321–2328.

https://doi.org/10.1039/c6sc04805f.

(2)   Lewis, J. C. Artificial Metalloenzymes and Metallopeptide Catalysts for Organic

Synthesis. *ACS Catal.* **2013**, *3*, 2954–2975. https://doi.org/10.1021/cs400806a.

(3)   Zhao, M.; Wang, H.-B.; Ji, L.-N.; Mao, Z.-W. Insights into Metalloenzyme

Microenvironments: Biomimetic Metal Complexes With a Functional Second

Coordination Sphere. *Chem. Soc. Rev.* **2013**, *42*, 8360–8375.

https://doi.org/10.1039/c3cs60162e.

(4)   Shook, R. L.; Borovik, A. S. Role of the Secondary Coordination Sphere in Metal-

Mediated Dioxygen Activation. *Inorg. Chem.* **2010**, *49*, 3646–3660.

https://doi.org/10.1021/ic901550k.

(5)   Estes, S. L.; Qiao, B.; Jin, G. B. Ion Association With Tetra-n-Alkylammonium Cations

Stabilizes Higher-Oxidation-State Neptunium Dioxocations. *Nat. Commun.* **2019**, *10* (1),

1–8. https://doi.org/10.1038/s41467-018-07982-5.

(6)   Wacker, J. N.; Nicholas, A. D.; Vasiliu, M.; Marwitz, A. C.; Bertke, J. A.; Dixon, D. A.;

Knope, K. E. Impact of Noncovalent Interactions on the Structural Chemistry of

Thorium(IV)-Aquo-Chloro Complexes. *Inorg. Chem.* **2021**.

https://doi.org/10.1021/acs.inorgchem.1c00099.

(7)   Singh, A.; Gelman, D. Cooperative Reactivity in Carbometalated Pincer-Type Complexes

Possessing an Appended Functionality. *ACS Catal. Catal.* **2020**, *10*, 1246–1255.

https://doi.org/10.1021/acscatal.9b04882.

(8)   Chatterjee, B.; Chang, W. C.; Jena, S.; Werlé, C. Implementation of Cooperative Designs
        in Polarized Transition Metal Systems-Significance for Bond Activation and Catalysis.
        ACS Catal. **2020**, *10* (23), 14024–14055. https://doi.org/10.1021/acscatal.0c03794.

(9)   A Hale, L. V; Szymczak, N. K. Hydrogen Transfer Catalysis Beyond the Primary
        Coordination Sphere. *ACS Catal.* **2018**, *8*, 6446–6461.
        https://doi.org/10.1021/acscatal.7b04216.

(10)   Trouve, J.; Gramage-Doria, R. Beyond Hydrogen Bonding: Recent Trends of Outer
        Sphere Interactions in Transition Metal Catalysis. *Chem. Soc. Rev.* **2021**, *50*, 3565–3584.

(11)   Dubois, M. R.; Dubois, D. L. The Roles of the First and Second Coordination Spheres in
        the Design of Molecular Catalysts for H2 Production and Oxidationw. *Chem. Soc. Rev.*
        2009, *9*, 62–72. https://doi.org/10.1039/b801197b.

(12)   S L V Narayana, Y.; Yoshida, T.; Chakraborty, C.; Bera, M. K.; Higuchi, M. Proton
        Conductivity of Metallo-Supramolecular Polymer Boosted by Lithium Ions. *ACS Appl.
        Polym. Mater.* **2020**, *2* (2), 326–334. https://doi.org/10.1021/acsapm.9b00818.

(13)   Herchel, R.; Zoufaí, P.; Nemec, I. The Effect of the Second Coordination Sphere on the
        Magnetism of $[Ln(NO_3)_3(H_2O)_3]$(18-Crown-6) (Ln = Dy and Er). *RSC Adv.* **2019**, *9*, 569–
        575. https://doi.org/10.1039/c8ra09648a.

(14)   Schulte, K. A.; Vignesh, K. R.; Dunbar, K. R. Effects of Coordination Sphere on
        Unusually Large Zero Field Splitting and Slow Magnetic Relaxation in Trigonally
        Symmetric Molecules. *Chem. Sci.* **2018**, *9*, 9018–9026.
        https://doi.org/10.1039/c8sc02820f.

(15)   Gebhard, M. S.; Koch, S. A.; Millar, M.; Devlin, F. J.; Stephens, P. J.; Solomon, E. I.
        Single-Crystal Spectroscopic Studies of $Fe(SR)_4{}^{2-}$ (R = 2-(Ph)C_6H_4): Electronic Structure

of the Ferrous Site in Rubredoxin. *J. Am. Chem. Soc* **1991**, *113*, 1640–1649.

(16) Forgan, R. S.; Roach, B. D.; Wood, P. A.; White, F. J.; Campbell, J.; Henderson, D. K.; Kamenetzky, E.; McAllister, F. E.; Parsons, S.; Pidcock, E.; Richardson, P.; Swart, R. M.; Tasker, P. A. Using the Outer Coordination Sphere to Tune the Strength of Metal Extractants. *Inorg. Chem.* **2011**, *50* (10), 4515–4522. https://doi.org/10.1021/ic200154y.

(17) Duan, W.-L.; Wang, H.-C.; Martí-Rujas, J.; Guo, F. Fluorescence-Based Detection of Nitroaromatics Using a Luminescent Second Sphere Adduct Self-Assembled by Charge-Assisted Hydrogen Bonds. *Cryst. Eng. Comm.* **2018**, *20*, 323–327. https://doi.org/10.1039/c7ce01743j.

(18) Park, Y.-S.; Dmytruk, A.; Dmitruk, I.; Kasuya, A.; Takeda, M.; Ohuchi, N.; Okamoto, Y.; Kaji, N.; Tokeshi, M.; Baba, Y. Size-Selective Growth and Stabilization of Small CdSe Nanoparticles in Aqueous Solution. *ACS Nano* **2010**, *4*, 121–128. https://doi.org/10.1021/nn901570m.

(19) Oktawiec, J.; Jiang, H. Z. H.; Vitillo, J. G.; Reed, D. A.; Darago, L. E.; Trump, B. A.; Bernales, V.; Li, H.; Colwell, K. A.; Furukawa, H.; Brown, C. M.; Gagliardi, L.; Long, J. R. Negative Cooperativity Upon Hydrogen Bond-Stabilized O_2 Adsorption in a Redox-Active Metal–Organic Framework. *Nat. Commun.* **2020**, *11*, 1–11. https://doi.org/10.1038/s41467-020-16897-z.

(20) Dalrymple, S. A.; Shimizu, G. K. H. Supramolecular Chemistry Exploiting Complementary Second-Sphere Effects in Supramolecular Coordination Solids. *Supramol. Chem.* **2003**, *15*, 591–606. https://doi.org/10.1080/10610270310001605188.

(21) Haaf, S.; Kaifer, E.; Wadepohl, H.; Himmel, H.-J. Use of Crown Ether Functions as Secondary Coordination Spheres for the Manipulation of Ligand-Metal Intramolecular

Electron Transfer in Copper-Guanidine Complexes. *Chem. Eur. J.* **2021**, *27*, 959–970. https://doi.org/10.1002/chem.202003469.

(22)   Deblonde, G. J. P.; Sturzbecher-Hoehne, M.; Rupert, P. B.; An, D. D.; Illy, M. C.; Ralston, C. Y.; Brabec, J.; De Jong, W. A.; Strong, R. K.; Abergel, R. J. Chelation and Stabilization of Berkelium in Oxidation State +IV. *Nat. Chem.* **2017**, *9*, 843–849. https://doi.org/10.1038/nchem.2759.

(23)   Baldwin, A. G.; Ivanov, A. S.; Williams, N. J.; Ellis, R. J.; Moyer, B. A.; Bryantsev, V. S.; Shafer, J. C. Outer-Sphere Water Clusters Tune the Lanthanide Selectivity of Diglycolamides. *ACS Cent. Sci.* **2018**, *4*, 739–747. https://doi.org/10.1021/acscentsci.8b00223.

(24)   Faizova, R.; Fadaei-Tirani, F.; Bernier-Latmani, R.; Mazzanti, M. Ligand-Supported Facile Conversion of Uranyl(VI) into Uranium(IV) in Organic and Aqueous Media. *Angew. Chemie* **2020**, *132* (17), 6822–6825. https://doi.org/10.1002/ange.201916334.

(25)   Andrez, J.; Bozoklu, G.; Nocton, G.; Pécaut, J.; Scopelliti, R.; Dubois, L.; Mazzanti, M. Lanthanide(II) Complexes Supported by N,O-Donor Tripodal Ligands: Synthesis, Structure, and Ligand-Dependent Redox Behavior. *Chem. Eur. J.* **2015**, *21* (43), 15188– 15200. https://doi.org/10.1002/chem.201502204.

(26)   Arnold, P. L.; Cowie, B. E.; Suvova, M.; Zegke, M.; Magnani, N.; Colineau, E.; Griveau, J. C.; Caciuffo, R.; Love, J. B. Axially Symmetric U−O−Ln- and U−O−U-Containing Molecules from the Control of Uranyl Reduction with Simple f-Block Halides. *Angew. Chemie - Int. Ed.* **2017**, *56* (36), 10775–10779. https://doi.org/10.1002/anie.201705197.

(27)   Dutkiewicz, M. S.; Apostolidis, C.; Walter, O.; Arnold, P. L. Reduction Chemistry of Neptunium Cyclopentadienide Complexes: From Structure to Understanding. *Chem. Sci.*

2017, *8*, 2553–2561. https://doi.org/10.1039/c7sc00034k.

(28) Jenks, T. C.; Kuda-Wedagedara, A. N. W.; Bailey, M. D.; Ward, C. L.; Allen, M. J.
Spectroscopic and Electrochemical Trends in Divalent Lanthanides through Modulation of
Coordination Environment. *Inorg. Chem.* **2020**, *59*, 2613–2620.
https://doi.org/10.1021/acs.inorgchem.0c00136.

(29) Etourneau, J.; Portier, J.; Ménil, F. The Role of the Inductive Effect in Solid State
Chemistry: How the Chemist Can Use It to Modify Both the Structural and the Physical
Properties of the Materials. *J. Alloys Compd.* **1992**, *188*, 1–7.

(30) Piro, N. A.; Robinson, J. R.; Walsh, P. J.; Schelter, E. J. The Electrochemical Behavior of
Cerium(III/IV) Complexes: Thermodynamics, Kinetics and Applications in Synthesis.
Coord. Chem. Rev. **2014**, *260*, 21–36.

(31) Robinson, J. R.; Qiao, Y.; Gu, J.; Carroll, P. J.; Walsh, P. J.; Schelter, E. J. The Role of
Dynamic Ligand Exchange in the Oxidation Chemistry of Cerium(III). *Chem. Sci.* **2016**,
7, 4537–4547.

(32) Willauer, A. R.; Palumbo, C. T.; Scopelliti, R.; Zivkovic, I.; Douair, I.; Maron, L.;
Mazzanti, M. Stabilization of the Oxidation State +IV in Siloxide-Supported Terbium
Compounds. *Angew. Chemie Int. Ed.* **2020**, *59*, 3549–3553.

(33) Laptev, D. M.; Kiseleva, T. V.; Kulagin, N. M.; Goryushkin, V. F.; Vorontsov, E. S. The
Thermal Decomposition of the Trichlorides of Lanthanides of the Cerium Sub-Group.
Russ. Jouranl Inorg. Chem. **1986**, *31*, 1131–1133.

(34) Gaune-Escard, M. Thermodynamics of Lanthanide Halides and Application to High-
Temperature Processes. *Scand. J. Metall.* **2005**, *34* (6), 369–375.
https://doi.org/10.1111/j.1600-0692.2005.00757.x.

(35)   Kwon, C.; Noh, S. H.; Chun, H.; Hwang, I. S.; Han, B. First Principles Computational Studies of Spontaneous Reduction Reaction of Eu(III) in Eutectic LiCl-KCl Molten Salt. *Int. J. Energy Res.* **2018**, *42* (8), 2757–2765. https://doi.org/10.1002/er.4064.

(36)   Novoselova, A.; Khokhlov, V.; Shishkin, V. Thermodynamic Characteristics of Samarium and Europium Chlorides in Molten Alkali Metal Chlorides. *Z. Naturforsch.* **2001**, *56*, 837–840.

(37)   Novoselova, A. V.; Smolenskii, V. V. Electrochemical and Thermodynamic Properties of Lanthanides (Nd, Sm, Eu, Tm, Yb) in Alkali Metal Chloride Melts. *Radiochemistry* **2013**, *55* (3), 243–256. https://doi.org/10.1134/S1066362213030016.

(38)   Kuznetsov, S.; Gaune-escard, M. Electrochemistry and Thermodynamics of $EuCl_3$ and $EuCl_2$ in Alkali Chloride Melts. *J. Nucl. Sci. Technol.* **2002**, *39*, 628–631. https://doi.org/10.1080/00223131.2002.10875546.

(39)   Kuznetsov, S. A.; Gaune-Escard, M. Kinetics of Electrode Processes and Thermodynamic Properties of Europium Chlorides Dissolved in Alkali Chloride Melts. *J. Electroanal. Chem.* **2006**, *595*, 11–22. https://doi.org/10.1016/j.jelechem.2006.02.036.

(40)   Kuznetsov, S. A.; Rycerz, L.; Gaune-Escard, M. Thermodynamics of Europium Chlorides in Alkali Chloride Melts. *J. New Mater. Electrochem. Syst.* **2006**, *9*, 313–321.

(41)   Schroll, C. A.; Chatterjee, S.; Levitskaia, T. G.; Heineman, W. R.; Bryan, S. A. Electrochemistry of Europium(III) Chloride in 3 LiCl – NaCl, 3 LiCl – 2 KCl, LiCl – RbCl, and 3 LiCl – 2 CsCl Eutectics at Various Temperatures. *J. Electrochem. Soc.* **2017**, *164* (8), H5345–H5352. https://doi.org/10.1149/2.0521708jes.

(42)   Duffy, J. A.; Ingram, M. D. Establishment of an Optical Scale for Lewis Basicity in Inorganic Oxyacids, Molten Salts, and Glasses. *J. Am. Chem. Soc.* **1971**, *93* (24), 6448–

6454. https://doi.org/10.1021/ja00753a019.

(43) Brooker, M. H.; Bredig, M. A. Significance of Both Polarizability and Polarizing Power of Cations in Nitrate Vibrational Spectra. *J. Chem. Phys.* **1973**, *58* (12), 5319–5321. https://doi.org/10.1063/1.1679146.

(44) Grégoire, B.; Ruby, C.; Carteret, C. Structural Cohesion of M^{II}-M^{III} Layered Double Hydroxides Crystals: Electrostatic Forces and Cationic Polarizing Power. *Cryst. Growth Des.* **2012**, *12* (9), 4324–4333. https://doi.org/10.1021/cg3006053.

(45) Song, J.; Wang, Q.; Kang, M.; Jiao, S.; Zhu, H. The Equilibrium Between Titanium Ions and Metallic Titanium in the Molten Binary Mixtures of LiCl. *Electrochemistry* **2014**, *82* (12), 1047–1051. https://doi.org/10.5796/electrochemistry.82.1047.

(46) Anderson, L. B.; Macero, D. J. The Formal Reduction Potential of the Europium(III)-Europium(II) System. *J. Am. Chem. Soc* **1936**, *88* (2), 1942–1942.

(47) Morss, L. R. Thermochemical Properties of Yttrium, Lanthanum, and the Lanthanide Elements and Ions. *Chem. Rev.* **1976**, *76* (6), 827–841. https://doi.org/10.1021/cr60304a007.

(48) Arashiba, K.; Kanega, R.; Himeda, Y.; Nishibayashi, Y. Electrochemical Reduction of Samarium Triiodide into Samarium Diiodide. *Chem. Lett* **2020**, *49*, 1171–1173. https://doi.org/10.1246/cl.200429.

(49) Fieser, M. E.; Ferrier, M. G.; Su, J.; Batista, E.; Cary, S. K.; Engle, J. W.; Evans, W. J.; Pacheco, J. S. L.; Kozimor, S. A.; Olson, A. C.; Ryan, A. J.; Stein, B. W.; Wagner, G. L.; Woen, D. H.; Vitova, T.; Yang, P. Evaluating the Electronic Structure of Formal Ln^{II} Ions in Ln^{II}-$(C_5H_4SiMe_3)^{3-}$ Using XANES Spectroscopy and DFT Calculations. *Chem. Sci.* **2017**, *8*, 6076–6091. https://doi.org/10.1039/c7sc00825b.

(50)   Meyer, G.; Wickleder, M. S. *Handbook on the Physics and Chemistry of Rare Earths, Volume 28 - 1st Edition*; Gschneider, K. A., Eyring, L., Eds.; Elsevier Science B. V., 2000.

(51)   Lissner, F.; Kraemer, K.; Schleid, T.; Meyer, G.; Hu, Z.; Kaindl, G. Die Chloride $Na_{3x}M_{2-x}Cl_6$ (M = La-Sm) Und NaM_2Cl_6 (M = Nd, Sm): Derivate Des UCl_3-Typs. Synthese, Kristallstruktur Und Roentgenabsorptionsspektroskopie (XANES). *Zeitschrift fuer Anorg. und Allg. Chemie* **1994**, *620* (3), 444–450. https://doi.org/10.1002/zaac.19946200307.

(52)   Hu, Z.; Kaindl, G.; Meyer, G. X-Ray Absorption Near-Edge Structure at the L_{I-III} Thresholds of Pr, Nd, Sm, and Dy Compounds With Unusual Valences. *J. Alloys Compd.* **1997**, *246*, 186–192.

(53)   Dahlén, A.; Hilmersson, G. Samarium(II) Iodide Mediated Reductions - Influence of Various Additives. *Eur. J. Inorg. Chem.* **2004**, No. 17, 3393–3403. https://doi.org/10.1002/ejic.200400442.

(54)   Molander, G. A. Reductions with Samarium(II) Iodide. In *Organic Reactions*; John Wiley & Sons, Inc.: Hoboken, NJ, USA, 2004; pp 211–367. https://doi.org/10.1002/0471264180.or046.03.

(55)   Beaurepaire, E.; Kappler, J. P.; Krill, G. X-Ray-Absorption Near-Edge Structure Study in Mixed-Valent Samarium Systems. *Phys. Rev. B* **1990**, *41*, 6768–6776.

(56)   Yoon, S.; Kang, D.; Sohn, S.; Park, J.; Choi, S.; Lee, M. Reference Electrode at Molten Salt: A Comparative Analysis of Electroceramic Membranes. *J. Nucl. Fuel Cycle Waste Technol.* **2020**, *18* (2), 143–155. https://doi.org/10.7733/jnfcwt.2020.18.2.143.

(57)   Al-Shara, N. K.; Sher, F.; Iqbal, S. Z.; Sajid, Z.; Chen, G. Z. Electrochemical Study of Different Membrane Materials for the Fabrication of Stable, Reproducible and Reusable

Reference Electrode. *J. Energy Chem.* **2020**, *49*, 33–41.

(58) Shirai, O.; Nagai, T.; Uehara, A.; Yamana, H. Electrochemical Properties of the Ag+|Ag and Other Reference Electrodes in the LiCl-KCl Eutectic Melts. *J. Alloys Compd.* **2008**, *456*, 498–502.

(59) Zhang, M.; Ge, J.; Zhang, J.; Liu, L. E. Redox Potential Measurement of AgCl in Molten LiCl-KCl Salt Using Chronopotentiometry and Potentiodynamic Scan Techniques. *Electrochem. commun.* **2019**, *105* (June), 106498. https://doi.org/10.1016/j.elecom.2019.106498.

(60) Janz, G. J. *Molten Salts Handbook*; Academic Press, 1967. https://doi.org/10.1016/b978-0-123-95642-2.x5001-1.

(61) Bhatt, A. I.; Snook, A. G. Chapter 7: Reference Electrodes for Ionic Liquids and Molten Salts. In *Handbook of Reference Electrodes*; Inzelt, G., Lewenstam, A., Scholz, F., Eds.; Springer-Verlag, 2013; pp 189–227.

(62) Kaya, S. Relationships Between Lattice Energies of Inorganic Ionic Solids. *Phys. B Condens. Matter* **2018**, *538*, 25–28.

(63) Cotton, S. A. *Lanthanide and Actinide Chemistry*; Woollins, D., Crabtree, B., Atwood, D., Meyer, G., Eds.; John Wiley & Sons, Ltd, 2006.

(64) Ferro, S.; De Battisti, A. Electrochemistry of the Aqueous Europium(III)/Europium(II) Redox Couple at Conductive Diamond Electrodes. *J. Electroanal. Chem.* **2002**, *533*, 177–180.

(65) Wang, Y.; Laborda, E.; Henstridge, M. C.; Martinez-Ortiz, F.; Molina, A.; Compton, R. G. The Use of Differential Pulse Voltammetries to Discriminate Between the Butler-Volmer and the Simple Marcus-Hush Models for Heterogeneous Electron Transfer: The

Electro-Reduction of Europium (III) in Aqueous Solution. *J. Electroanal. Chem.* **2012**, *668*, 7–12. https://doi.org/10.1016/j.jelechem.2011.12.023.

(66)   Iwadate, Y. Structures and Properties of Rare-Earth Molten Salts. In *Handbook on the Physics and Chemistry of Rare Earths, Vol. 44*; Bunzli, J.-C., Pecharsky, V., Eds.; North-Holland, 2012; pp 87–168.

(67)   Smirnov, P. R.; Trostin, V. N. Structural Parameters of the Nearest Surrounding of Lanthanide Ions in Aqueous Solutions of Their Salts. *Russ. J. Gen. Chem.* **2012**, *82* (3), 366–384. https://doi.org/10.1134/S1070363212030036.

(68)   Tanaka, F.; Yamashita, S. Luminescence Lifetimes of Aqueous Europium Chloride, Nitrate, Sulfate, and Perchlorate Solutions. Studies on the Nature of the Inner Coordination Sphere of the Europium(III) Ion. *Inorg. Chem* **1984**, *23*, 2044–2046.

(69)   Ferrier, M. G.; Batista, E. R.; Berg, J. M.; Birnbaum, E. R.; Cross, J. N.; Engle, J. W.; La Pierre, H. S.; Kozimor, S. A.; Pacheco, J. S. L.; Stein, B. W.; Stieber, S. C. E.; Wilson, J. J. Spectroscopic and Computational Investigation of Actinium Coordination Chemistry. *Nat. Commun.* **2016**, *7*, 1–8. https://doi.org/10.1038/ncomms12312.

(70)   Allen, P. G.; Bucher, J. J.; Shuh, D. K.; Edelstein, N. M.; Craig, I. Coordination Chemistry of Trivalent Lanthanide and Actinide Ions in Dilute and Concentrated Chloride Solutions. *Inorg. Chem.* **2000**, *39*, 595–601. https://doi.org/10.1021/ic9905953.

(71)   Ravel, B.; Newville, M. Synchrotron Radiation ATHENA, ARTEMIS, HEPHAESTUS: Data Analysis for X-Ray Absorption Spectroscopy Using IFEFFIT. *J. Synchrotron Rad* **2005**, *12*, 537–541. https://doi.org/10.1107/S0909049505012719.

(72)   Cramer, C. J.; Truhlar, D. G. Implicit Solvation Models: Equilibria, Structure, Spectra, and Dynamics. *Chem. Rev.* **1999**, *99* (8), 2161–2200. https://doi.org/10.1021/cr960149m.

(73) Steele, H. M.; Guillaumont, D.; Moisy, P. Density Functional Theory Calculations of the Redox Potentials of Actinide(VI)/Actinide(V) Couple in Water. *J. Phys. Chem. A* **2013**, *117* (21), 4500–4505. https://doi.org/10.1021/jp401875f.

(74) Wang, Z.; Yan, L.; Yue, B.; Jiang, T.; Peng, S.; Lv, W.; Zhang, D. Density Functional Theory Calculations of Redox Potentials of Neptunium Complexes in Ionic Liquid. *J. Electrochem. Soc.* **2020**, *167* (13), 136503. https://doi.org/10.1149/1945-7111/abb6c9.

(75) Roy, L. E.; Jakubikova, E.; Guthrie, M. G.; Batista, E. R. Calculation of One-Electron Redox Potentials Revisited. Is It Possible to Calculate Accurate Potentials with Density Functional Methods? *J. Phys. Chem. A* **2009**, *113* (24), 6745–6750. https://doi.org/10.1021/jp811388w.

(76) Andrade, G. A.; Popov, I. A.; Federico, C. R.; Yang, P.; Batista, E. R.; Mukundan, R.; Davis, B. L. Expanding the Potential of Redox Carriers for Flow Battery Applications. *J. Mater. Chem. A* **2020**, *8* (34), 17808–17816. https://doi.org/10.1039/D0TA04511J.

(77) Kresse, G.; Furthmüller, J. Efficient Iterative Schemes for Ab Initio Total-Energy Calculations Using a Plane-Wave Basis Set. *Phys. Rev. B* **1996**, *54* (16), 11169–11186. https://doi.org/10.1103/PhysRevB.54.11169.

(78) Kresse, G.; Furthmüller, J. Efficiency of Ab-Initio Total Energy Calculations for Metals and Semiconductors Using a Plane-Wave Basis Set. *Comput. Mater. Sci.* **1996**, *6* (1), 15–50. https://doi.org/10.1016/0927-0256(96)00008-0.

(79) Kresse, G.; Joubert, D. From Ultrasoft Pseudopotentials to the Projector Augmented-Wave Method. *Phys. Rev. B* **1999**, *59* (3), 1758–1775. https://doi.org/10.1103/PhysRevB.59.1758.

(80) Blöchl, P. E. Projector Augmented-Wave Method. *Phys. Rev. B* **1994**, *50* (24), 17953–

17979. https://doi.org/10.1103/PhysRevB.50.17953.

(81)   Perdew, J. P.; Burke, K.; Ernzerhof, M. Generalized Gradient Approximation Made
       Simple. *Phys. Rev. Lett.* **1997**, *78* (7), 1396–1396.
       https://doi.org/10.1103/PhysRevLett.78.1396.

(82)   Grimme, S.; Antony, J.; Ehrlich, S.; Krieg, H. A Consistent and Accurate Ab Initio
       Parametrization of Density Functional Dispersion Correction (DFT-D) for the 94
       Elements H-Pu. *J. Chem. Phys.* **2010**, *132* (15), 154104.
       https://doi.org/10.1063/1.3382344.

(83)   Nosé, S. A Unified Formulation of the Constant Temperature Molecular Dynamics
       Methods. *J. Chem. Phys.* **1984**, *81* (1), 511–519. https://doi.org/10.1063/1.447334.

(84)   Hoover, W. G. Canonical Dynamics: Equilibrium Phase-Space Distributions. *Phys. Rev. A*
       1985, *31* (3), 1695–1697. https://doi.org/10.1103/PhysRevA.31.1695.

(85)   Nam, H. O.; Morgan, D. Redox Condition in Molten Salts and Solute Behavior: A First-
       Principles Molecular Dynamics Study. *J. Nucl. Mater.* **2015**, *465*, 224–235.
       https://doi.org/10.1016/j.jnucmat.2015.05.028.

(86)   Henkelman, G.; Arnaldsson, A.; Jónsson, H. A Fast and Robust Algorithm for Bader
       Decomposition of Charge Density. *Comput. Mater. Sci.* **2006**, *36* (3), 354–360.
       https://doi.org/10.1016/j.commatsci.2005.04.010.

(87)   Shannon, R. D. *Revised Effective Ionic Radii and Systematic Studies of Interatomic
       Distances in Halides and Chalcogenides*; 1976; Vol. 32.